Citation: Zhaokun Ren, Zhanyuan Ma, Xiaozhe Shi, et al.Investigation and mechanical behavior analysis of automatic deformable deflector based on smart materials. *Journal of Harbin Institute of Technolgoy(New Series)*,DOI:10.11916/j.issn.1005-9113.24026

Investigation and Mechanical Behavior Analysis of Automatic Deformable Deflector Based on Smart Materials

Zhaokun Ren, Zhanyuan Ma, Xiaozhe Shi, Shiyu Zhang and Chen Bu*

(*AVIC Aerodynamic Research Institute, Harbin 150001, China*)

Abstract: Smart materials, especially shape memory composites and 4D printing materials, are widely used in aerospace. Deflectors are essential equipment in wind tunnel construction. Traditional deflectors are made of metal materials and have a relatively high structural weight. The deflector made of smart material has the advantage of being lighter in weight compared to traditional structure, and it could change the bending angle of the deflector structure under external excitation. In this study, the corresponding mechanical property test and finite element simulation of the smart material are carried out, and the deflector made of smart material is further studied and analyzed. Maxwell viscoelasticity model for the material is established, and relevant parameters are obtained through stress relaxation test fitting. According to relevant parameters and literature, finite element simulation of intelligent deflector structure is carried out. The pressure loss coefficient, airflow deflection angle, and velocity uniformity are studied. The numerical model of the minimum pressure loss coefficient is established with reference to the relevant data, and the formula for calculating the optimal upwind radius of the deflector is obtained. Combined with the numerical simulation results of the flow deflection angle and velocity uniformity of the flow field, it provides a reference for the selection of the size of the deflector.

Keywords: deflector; smart materials; mechanical behavior; simulation; loss coefficient

CLC number: TB34 **Document code**: A **Article ID**: 1005-9113(2024)00-0000-15

0 Introduction

In the contemporary society, smart materials are very important, which include shape memory composites and materials used for 4D printing, and shape-memory polymer are mainly applied in aerospace, while 4D printing materials are mainly used in bioremediation and other fields[1-4]. Generally, smart materials need to be driven by external excitation, such as thermal, electrical, optical, magnetic, etc.[5-7]. Shape memory composite materials are mainly applied in space deployable structures in the aerospace field[8-12]. 4D printing materials are mainly used in the biological field, such as preparing printed vascular stents and plugging devices[13-21].

As the essential structure in wind tunnel testing, the deflector plays an irreplaceable role. In the field of aerospace, the lightweighting of structures is the trend of future development. Traditional deflectors, made of metal materials such as stainless steel, are unable to rotate after installation and have a large structural weight. The deflector made of smart material has a small structural density and can obtain the required deformation angle by external excitation. The deformation mechanism of the smart material is shown in Fig.1. In the initial state, the smart material is in the stretching state, and the ambient temperature is lower than the deformation temperature T_c. When the material is heated to a temperature higher than the transition temperature, an external load is applied to form the structure into a curved shape, in the meantime, the external load is maintained and the material temperature is reduced. After the material shape is fixed, the external load is unloaded. When the material is heated up to the transition temperature, the shape of smart material will be recovered.

Received 2024-04-26.

* Corresponding author. Zhaokun Ren, Ph.D. Email: dakun2008@163.com.

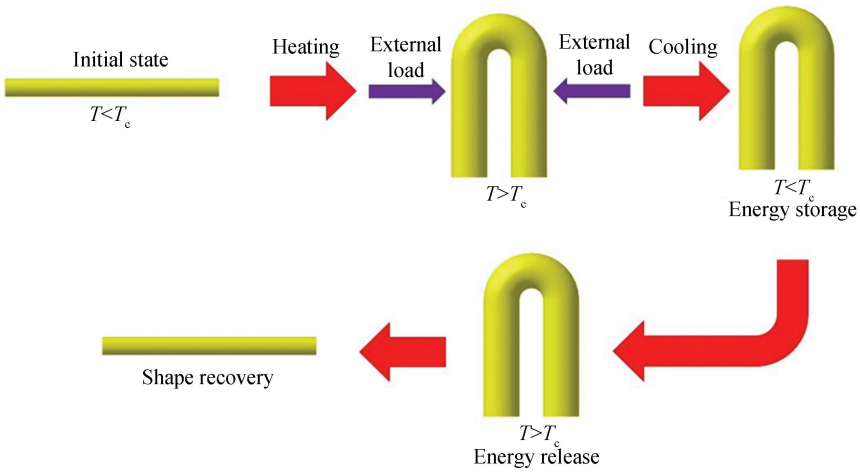

Fig.1 Deformation mechanism of smart material

1 Structure Design

Because the smart material studied at this stage only has the characteristics of unidirectional deformation, it is necessary to carry out corresponding structural design to realize the bidirectional deformation ability of the deflector. The deflector is composed of two lamellar structures prepared based on smart material, and the lamellar structure of smart material follows the deformation mechanism shown in Fig.1. Due to ensure the ability of the structure to undergo bidirectional deformation, two structures with different initial shapes were designed during the preparation of layered materials, namely the inner layer and outer layer. In the initial state, the inner layer prepared is a structure with a certain bending angle, while the outer layer prepared is a straight plate structure without bending, as shown in Fig.2.

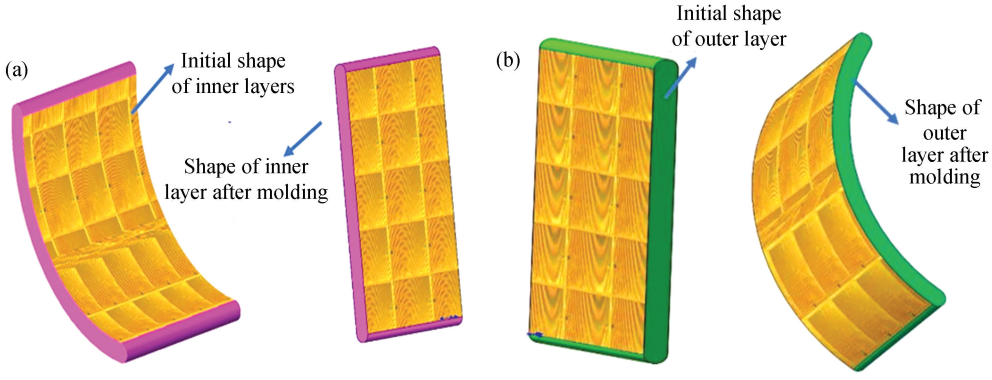

Fig.2 (a) The initial shape of the inner layer and the shape after molding; (b) The initial shape of the outer layer and the shape after molding

Heat the inner layer, which has a certain bending angle, to the glass transition temperature and then cool it. The inner layer is shaped into a straight plate, and then the inner layer and the outer layer are fixed together in their initial straight plate shape. Paste an electric heating film on the outermost surface of the inner layer and on the outer surface of the outer layer to control the temperature of the intelligent layer structure. When the deformation of the deflector is required, the electric heating film is activated, in the meantime, the inner layer has a tendency to return to its initial bending angle after reaching the glass transition temperature. At the same time, the temperature of the outer layer reaches the glass transition temperature, and its stiffness rapidly decreases. It is driven by the inner layer to deform and become a deflector with a certain bending angle. After the deflector reaches the required deformation angle,

the power supply of the electric heating film is turned off, causing the temperature of the smart layer material to drop below the glass transition temperature and the shape to become fixed. If the deflector is required to return to the straight plate state, the electrically heated film needs to be electrically heated again. Simultaneously, the temperature of the smart material lamella rises to the glass transition temperature, and the outer layer has a tendency to return to the original straight plate shape, while the inner layer also softens under the effect of high temperature, and the stiffness decreases significantly. The inner layer deforms to the straight plate shape together under the driving effect of the outer layer. Stop heating the electric heating film and quickly cool it down. The shape of the deflector is fixed to a straight plate, as shown in Fig.3.

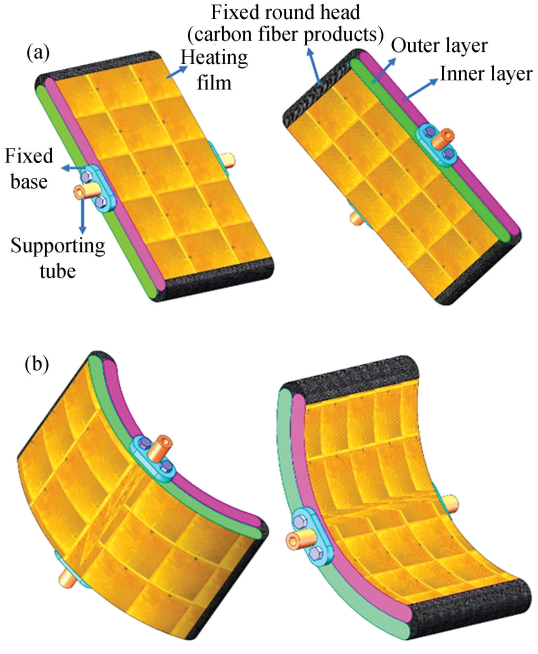

Fig.3 (a) Flow deflector in straight plate state; (b) Deflector in curved state

When preparing the inner layer, a layer with an initial shape with a certain bending angle is prepared firstly, then heat it to form a straight plate shape, and stick an electric heating film on the surface, as shown in Fig.2. When preparing the outer layer, the initial shape is a straight plate, and then the inner layer of the straight plate type and the outer layer of the straight plate type are bonded together, with the heating film on both sides exposed to the outside. In order to fix the two layers, a fixed round head made of carbon fiber is used to fix them.

Fixed bases are installed on the left and right sides of the deflector, and support tubes are installed to support the operation of the deflector. On the other hand, the wires of the electric heating film are led out through support tubes and connected to the control circuit. After electrification of the electric heating film, the intelligent layer is heated to the glass transition temperature by the electric heating film, and the guide vane gradually becomes a certain curved shape. After reaching a certain bending angle, stop heating and quickly cool down, and fix the guide vane into a certain bending shape. If it is necessary to return to the straight plate type, the electric heating film should be energized again to heat it until the glass transition temperature is reached. The guide vane gradually returns to the straight plate type, and then the power should be cut off again to stop heating and quickly cool down. The smart material could be selected according to different engineering requirements, such as PLA (polylactic acid), epoxy resin and other polymers that can deform. On the other hand, in order to improve the stiffness and strength of materials, carbon fiber, glass fiber or other nano particles could be used to strengthen polymers. For the bending angle of the deflector, design and preparation could be carried out during layer preparation and molding according to engineering requirements.

2 Analysis of Mechanical Properties on Smart Material

The intelligent material used in the paper is PLA, and the size of the material mechanical performance test sample prepared refers to the standard ASTM-D3039. The sample size is 115 mm×19 mm×2 mm, with a middle area size of 33 mm×6 mm×2 mm. In Fig.4, the tensile test curve is shown, and the expressions for true stress and true strain are as follows[22]:

$$\sigma_1 = \sigma_2(1 + \varepsilon_2) \quad (1)$$

$$\varepsilon_1 = \ln(1 + \varepsilon_2) \quad (2)$$

where σ_1 is true stress, ε_1 is true strain, ε_2 is engineering strain, σ_2 is engineering stress.

In Fig.4(a), the stress-strain curve of the sample, under 25 ℃ test temperature and different tensile rates, is shown. When the tensile rate is 2 mm/min, the axial stiffness of the sample is higher, and the axial stiffness under other tensile rates is relatively close. In Fig.4(b), the stress-strain curve

obtained at a tensile rate of 2 mm/min under different test temperatures is shown. E_1 – E_4 represent the tensile moduli of the sample at different temperatures of 25 ℃, 40 ℃, 50 ℃, and 60 ℃, respectively. The tensile modulus of he sample decreases continuously with the increase of test temperature. When the test temperature is 60 ℃, the modulus of the sample decreases rapidly. According to the information in Ref. [23], it is further confirmed that the glass transition temperature of the sample is approximately 60 ℃.

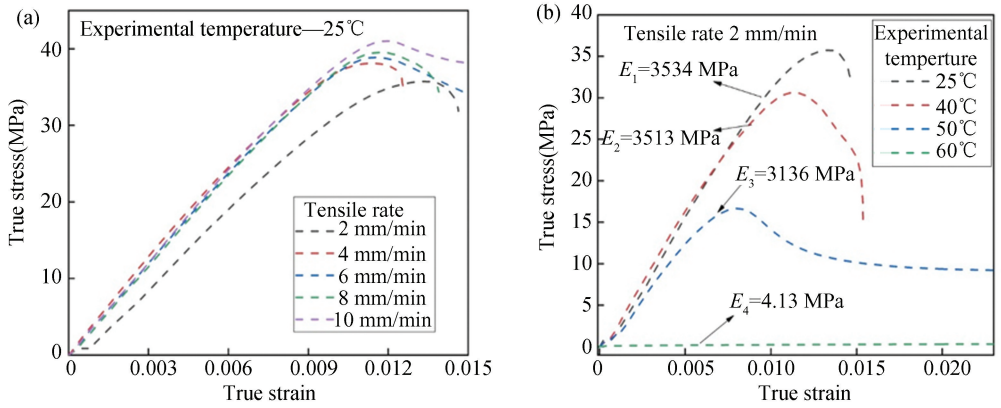

Fig.4 (a) Stress-strain curve under different tensile rates at 25 ℃; (b) Stress-strain curve with 2 mm/min tensile rate (25 ℃, 40 ℃, 50 ℃, 60 ℃)

In the paper, the Generalized Maxwell Model (GMM) is used to establish the viscoelastic relationship equation of the sample[23-24], as shown in Fig.5. E and E_1 – E_n are the tensile moduli of the respective Maxuell models. The model is composed of multiple Maxwell models in parallel, and each Maxwell model is composed of a dash pot and a spring in series, where the spring represents the elastic behavior of the material, and the dash pot represents the viscous behavior of the material. The relaxation time applied in the model has a distribution characteristic.

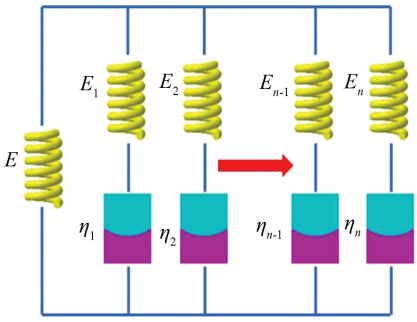

Fig.5 Schematic diagram of the generalized Maxwell model

In the paper, five parallel Maxwell models are used. The viscoelastic stress (σ) of the model mainly consists of two parts, one is related to strain ($\sigma_0(\varepsilon)$), and the other is related to time ($g(t)$). The expression is given by:

$$\sigma(\varepsilon,t)=\sigma_0(\varepsilon)\cdot g(t) \tag{3}$$

The modulus of the model is represented by the Prony order:

$$G(t)=G_0\left(g_\infty+\sum_{i=1}^{n}g_i\exp\left(\frac{-t}{\tau_i}\right)\right) \tag{4a}$$

$$K(t)=K_0\left(k_\infty+\sum_{i=1}^{n}k_i\exp\left(\frac{-t}{\tau_i}\right)\right) \tag{4b}$$

where G_0 and K_0 are instantaneous shear modulus and instantaneous bulk modulus respectively. $G(t)$ and $K(t)$ are the time varying shear modulus and relaxation modulus, respectively. g_∞, g_i, k_∞ and k_i are all dimensionless constants. In Eq. (3), $\sigma_0(\varepsilon)$ represents the stress-strain relationship at the initial moment, while $g_\infty\sigma_0(\varepsilon)$ represents the stress-strain relationship when the relaxation modulus reaches equilibrium. In the model, when the experimental temperature is much lower than the glass transition temperature, the material mainly exhibits elastic behavior. In order to characterize the viscoelastic behavior of materials at different temperatures, the time temperature equivalence principle is adopted in the model. The principle is based on the viscoelastic behavior at a reference temperature, which is related to the mechanical behavior at another temperature by changing the test time. The expression is given by Ref. [23]:

$$E(T,t) = E\left(T_0, \frac{t}{a_T}\right) = E(T_0, \log t - \log a_T) \tag{5}$$

where E represents the relaxation modulus; T_0 is reference temperature; t is test time, a_T is the displacement factor and a function of temperature, which is expressed using the WLF equation as follows:

$$\frac{1}{\log a_T} = -\frac{1}{C_1} - \frac{C_2}{C_1(T - T_0)} \tag{6}$$

In order to further study and analyze the model, stress relaxation tests were conducted on the samples at different temperatures, and relevant parameters were obtained to further analyze the deformation mechanism of the deflector. Therefore, tensile relaxation tests could be applied to obtain the change curve of relaxation modulus, and the relevant expression is given by:

$$G = \frac{E}{2(1+\mu)} \tag{7}$$

$$K = \frac{E}{3(1-2\mu)} \tag{8}$$

where μ is the Poisson's ratio, which is set to 0.35 in the paper. The parameters C_1 and C_2 in Eq. (6) are taken as 17.44 and 51.6, respectively.

Before conducting stress relaxation tests, it is necessary to preheat the sample for a certain period of time to ensure that the material and test environment can fully reach the required temperature.

In the paper, the tensile displacement applied in the stress relaxation test is 1 mm. On the other hand, for the accuracy, the test is conducted after maintaining the test temperature for 15 min. The test temperatures were 25, 35, 45, 55, and 60 ℃, respectively, and the test time was 1800 s. As shown in Fig. 6, under the test temperatures of 25 ℃ and 35 ℃, the relaxation stress of the sample continuously decreases with the increase of relaxation time, but the slope of the curve decrease is relatively gentle compared to the test temperatures of 55 ℃ and 60 ℃. In the initial state, as the test temperature increases, the initial stress continuously decreases. Moreover, when the test temperature is between 55 ℃ with 60 ℃, the relaxation equilibrium is reached within 100 s, and the relaxation stress no longer changes, which indicates that as the test temperature increases, the viscosity characteristics of the sample is the main manifestation to prove that the glass transition temperature of the sample is approximately 60 ℃.

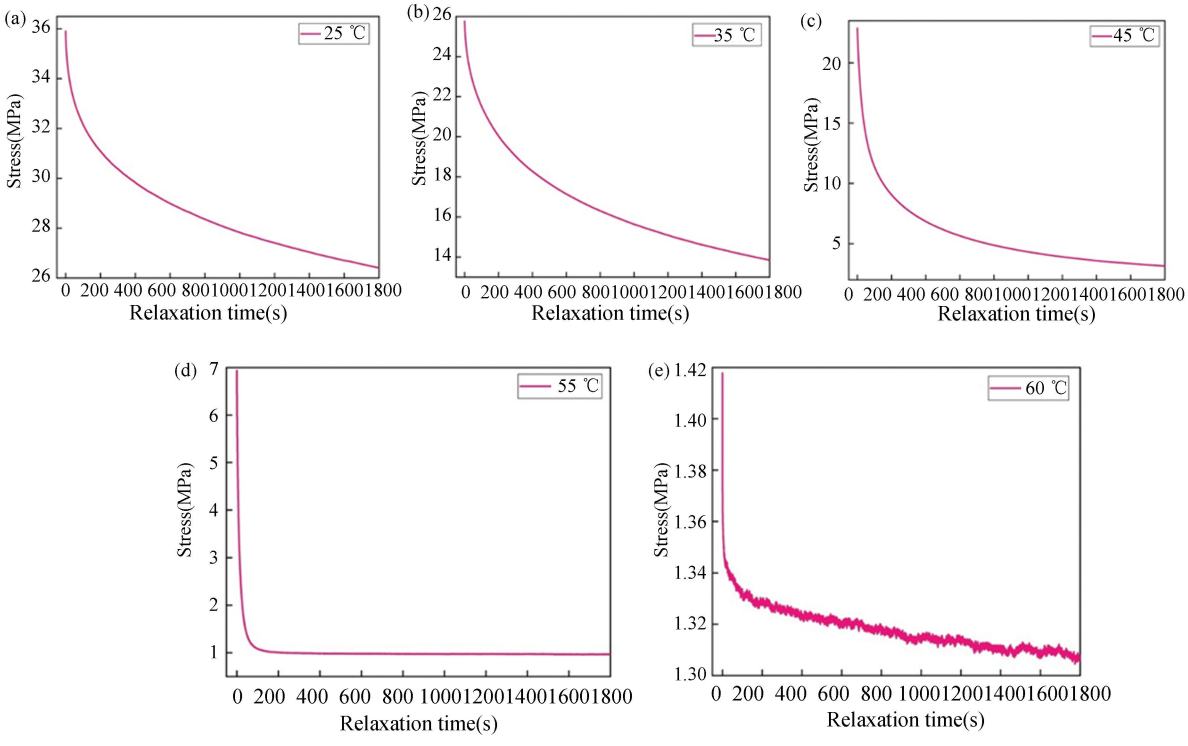

Fig.6 Stress relaxation curves at different temperatures with a pull-down displacement of 1 mm: (a) 25 ℃; (b) 35 ℃; (c) 45 ℃; (d) 55 ℃; (e) 60 ℃

In order to further study the stress relaxation behavior of the sample, the relationship between the relaxation modulus and the relaxation time is comprehensively analyzed in the paper. In Fig.7, the relaxation stress-strain curve of Fig. 6 was further processed to obtain the curve of material relaxation modulus changing with relaxation time. On the other hand, in order to further study the behavior of relaxation modulus variation, logarithmic processing was performed on the relaxation modulus and relaxation time in Fig.7. It can be seen from Fig.7 that the relaxation modulus decays significantly at 55 ℃ and 60 ℃. The purpose of logarithmic processing of relaxation modulus time is to further analyze by using the equivalence principle of time and temperature, and then obtain the fitting parameters of relevant models. Five parallel Maxwell models to characterize the multiple relaxation process is applied, and the model uses viscoelastic Prony order numbers to express it. By fitting Eq.(4) with the curve relationship between relaxation modulus and time in Fig.7, the relevant g_i is obtained, while τ_i is taken as 0.1, 1, 10, 100, 1000 s. The thermal expansion coefficient of this material is based on relevant literature, with $\alpha = 0.00017$, and other corresponding parameters are fitted using stress relaxation experimental data at 60 ℃. Bring the fitted parameters into the simulation program to simulate the deformation behavior of the material, assuming that C_1, C_2 and the thermal expansion coefficient remain constant. The simulation process for the deflector mainly includes four steps, as shown in Table 1.

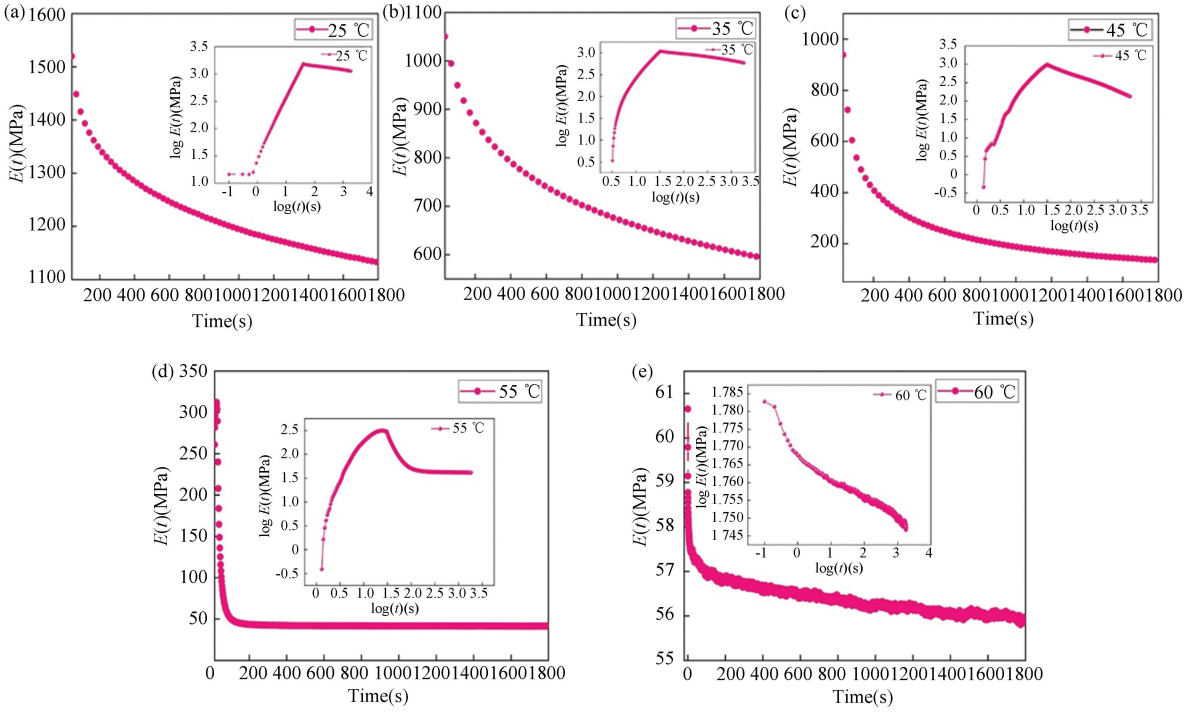

Fig.7 Time dependent curve of relaxation modulus on samples at different experimental temperatures: (a) 25 ℃; (b)35 ℃; (c)45 ℃; (d)55 ℃; (e) 60 ℃

Table 1 Setting of analysis steps

Analysis step number	Analysis step settings	Test temperature(℃)
1	Applying load	60
2	Maintain load and cool down	25
3	Maintain temperature and unload	25
4	Raise the temperature until the shape returns	60

In the initial state, the temperature of the deflector is raised to 60 ℃. Since the bending angle of the deflector is generally ca. 95°, which could be determined according to the requirement. In the second step, keep the load of the bending angle and reduce the temperature of the sample to 25 ℃. In the meantime, the molecular chain of the smart material used to prepare the deflector freezes. In the third step,

while maintaining the temperature constant, the load is removed. Due to the freezing of the material molecular chains, the structure of deflector no longer changes. In the fourth step, increasing the sample temperature causes the material's molecular chains to thaw and the shape of the deflector to recover.

Finite element analysis of the deformation process on the deflector is required, and the simulation results are shown in Fig. 8. The maximum and minimum Mises stress distribution is shown in Fig. 8 (a) and (b), during the deformation process of the deflector at different time steps. In Figs.8 (c) – (f), the stress distribution cloud maps during the simulation process of the deflector are partially shown. As shown in Fig.8 (a), as the deformation angle of the deflector increases, the maximum Mises stress gradually increases until the bending angle reaches 95 °, and the maximum stress peaks. As the deflector undergoes shape recovery when heated, the maximum Mises stress gradually decreases as the bending angle decreases. Compared to Fig.8 (b), the stress variation trend is relatively consistent. As shown in Fig.8 (c) – (f), the maximum Mises stress is mainly distributed at the root of the deflector, and when the bending angle reaches a certain value, the maximum stress area will transfer to the middle area of the deflector. Therefore, the bending part of the deflector can be reinforced to prevent the stress from exceeding the corresponding strength of the material and causing fatigue damage when designing the specific structure of the deflector.

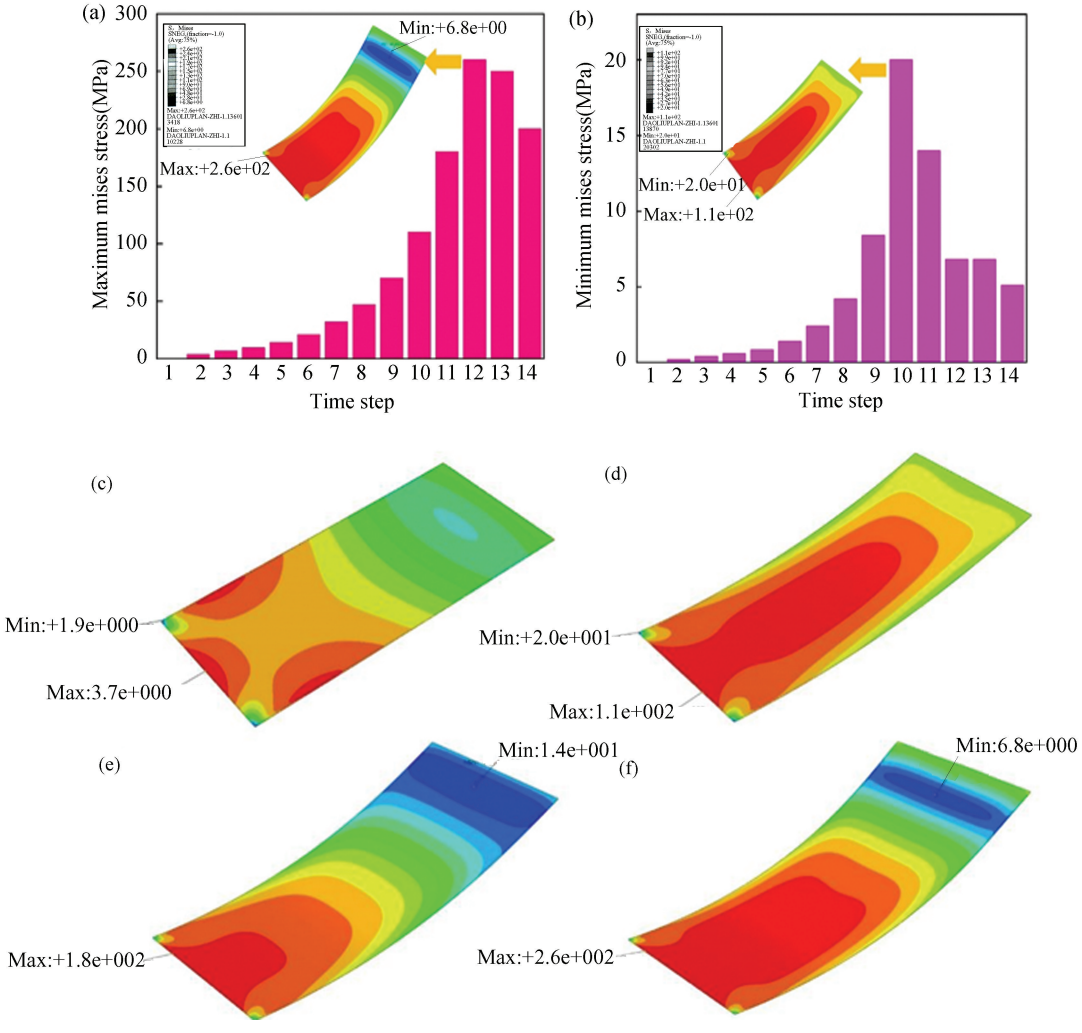

Fig.8 Mises stress distribution during the deformation process of the deflector; (a) Maximum Mises stress of the deflector at different time steps; (b) Minimum Mises stress of the deflector at different time steps; (c) – (f) Mises stress distribution cloud map of the deflector with partial time steps

3 Evaluation of the Working Effect of Deformable Deflector Array

The deflector is generally worked in the form of an array. By designing the deformable deflector, the required wind direction and other requirements can be met by controlling the deformation angle of each deflector, which is an advantage that other traditional deflector arrays has unpossessed advantages. In Fig.9, the workflow of a deformable deflector array is shown. Each deformable deflector could undergo deformation under electric heating excitation, and the deformation angle of each deflector is continuously adjusted through a controlling program until a specific flow field quality is produced.

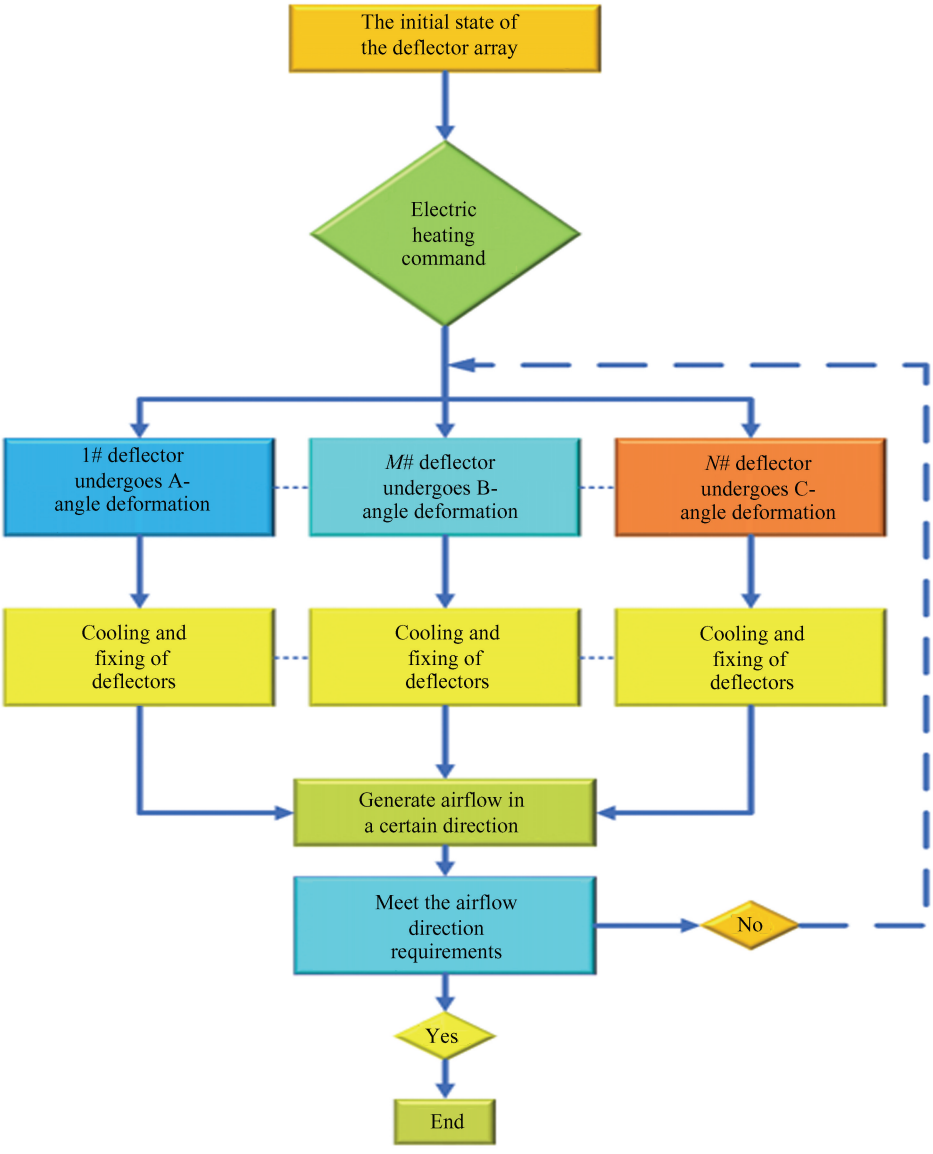

Fig.9 The controlling process of a deformable deflector array

An important factor in evaluating the quality of the flow field is the loss coefficient, which determines the distribution and size of the deflector based on the total pressure drop at the inlet and outlet. The generation of pressure loss is mainly caused by airflow friction loss, especially in turning, diversion, diffusion, contraction and other parts, as well as passing through devices such as grids, throttling, and porous media. At these positions, the momentum exchange between fluids is intensified, thereby increasing the degree of related pressure loss. The energy loss generated during the flow process is represented by the total pressure drop ΔP_0, and the pressure loss coefficient of this process is represented

by K. The relevant equation is as follows:

$$\Delta P_0 = P_1 - P_2 = K \cdot \frac{1}{2}\rho v^2 \quad (9)$$

where P_1 represents the total inlet pressure (Pa); P_2 is the total outlet pressure (Pa); ρ is air density (kg/m^3); v is airflow velocity (m/s).

In addition to the loss coefficient, another evaluation criterion is the airflow deflection angle in the flow field, and relevant regulations require the airflow deflection angle to not exceed ±0.5 °. The two-dimensional model is used to calculate the distribution of relevant flow fields, and according to relevant requirements, 75% of the center area of the airflow is applied as the reference domain for data analysis.

The paper focus on the preparation of flow deflectors based on smart materials. It is hoped that through a combination of numerical simulation and theoretical analysis, the effect of size variation on pressure loss coefficient and airflow deviation angle can be studied by changing the windward size of deformable flow deflectors.

The distribution, size, and mesh division of the deformable flow deflector are shown in Fig.10. The numerical simulation model used in the paper is the SST k-omega model, with boundary conditions of velocity inlet and pressure outlet. Using unstructured grids for partitioning models, the number of grids ranges from 200000 to 300000. According to relevant information, the deflector used in this simulation has a 95 ° angle, an equivalent corner diameter of L, a deflector thickness of h, and a windward radius of r.

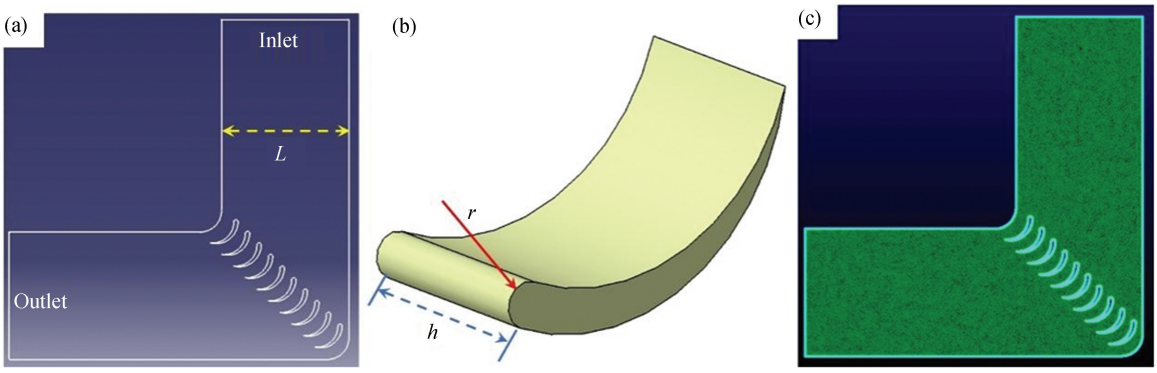

Fig.10 (a) Distribution diagram of flow deflector; (b) Schematic diagram of thickness and windward radius of deflector; (c) Schematic diagram of the two-dimensional grid of the model

In the paper, numerical simulations were conducted on the velocity distribution of the flow field with different radius under the condition of an inlet velocity of 10 m/s. The velocity cloud map of the flow field is shown in Fig. 11. As shown in Fig.11(a), without a deflector, the airflow generates large vortices and the velocity distribution is extremely uneven, resulting in significant energy loss. After installing the deflector, it can be clearly seen that the uniformity of air flow distribution has been greatly improved. However, when the radius of the deflector increases to a certain value (especially after 8 mm), the uniformity of air flow velocity distribution continues to decrease, and air flow separation and turbulence phenomena occur near the deflector, which indicates that a larger windward does not necessarily mean better airflow quality.

In Fig. 12, the numerical simulation results of pressure loss coefficients generated by deflectors with different radius under the inlet speed of 10 m/s are shown. At the same time, in order to study the changes of pressure loss coefficient under different speeds (Reynolds number), the deflectors with different radius (1.5, 3.5, 5.5, 7.5, 9.5 mm) were selected as the research objects in the paper, and the changing trend of the pressure loss coefficient was observed. As shown in Fig.12(a), with the increase of the deflector radius, the pressure loss coefficient presents an exponential rise, which is caused by the increase of the upwind radius of the deflector, resulting in the increase of airflow obstruction. In Fig.12(b)-(f), it can be seen that with the increase of inlet air velocity (Reynolds number), the pressure loss coefficient presents an exponential decline trend.

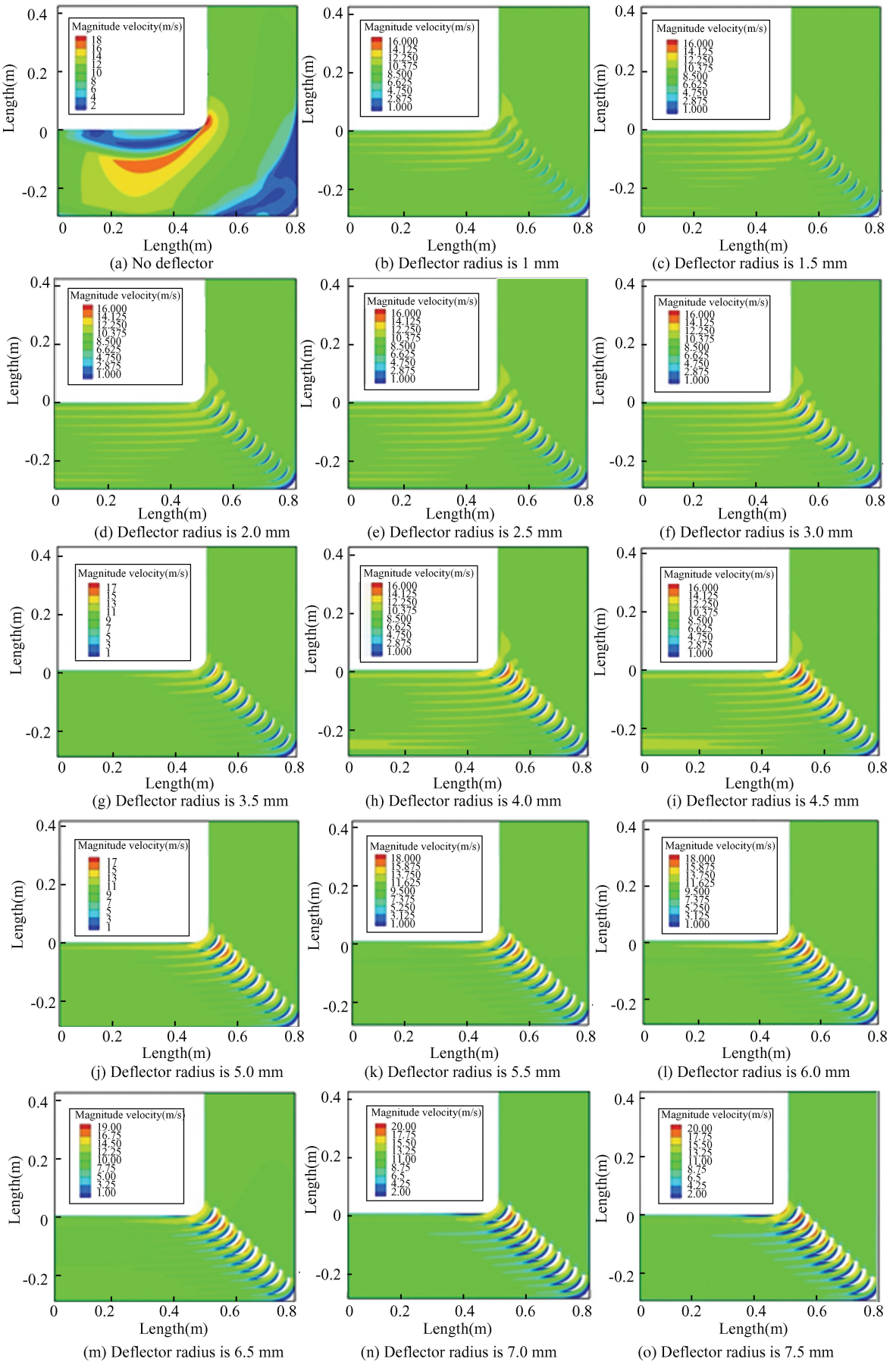

(a) No deflector (b) Deflector radius is 1 mm (c) Deflector radius is 1.5 mm

(d) Deflector radius is 2.0 mm (e) Deflector radius is 2.5 mm (f) Deflector radius is 3.0 mm

(g) Deflector radius is 3.5 mm (h) Deflector radius is 4.0 mm (i) Deflector radius is 4.5 mm

(j) Deflector radius is 5.0 mm (k) Deflector radius is 5.5 mm (l) Deflector radius is 6.0 mm

(m) Deflector radius is 6.5 mm (n) Deflector radius is 7.0 mm (o) Deflector radius is 7.5 mm

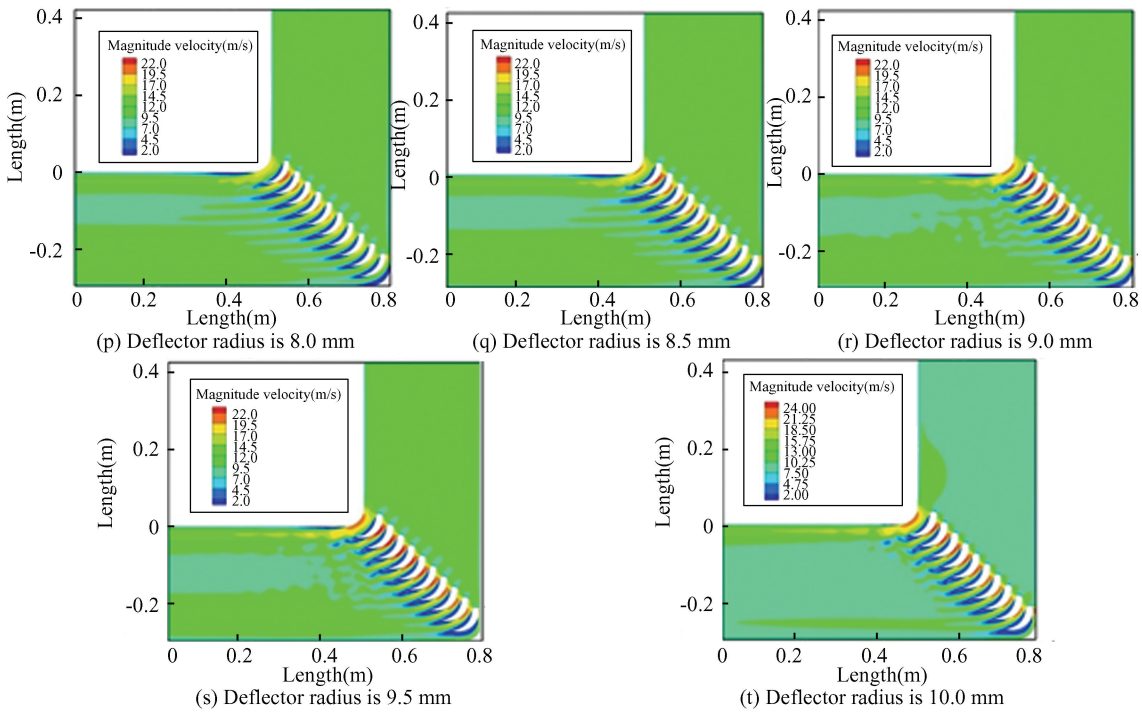

Fig.11 The effect of different deflector radius on velocity distribution under the inlet velocity of 10 m/s

However, in the process of specific engineering applications, the results obtained by CFD calculation often have certain deviations. When different kinds of numerical models are used for simulation, the results will be very different, so it is necessary to refer to some empirical formulas for reference and correction.

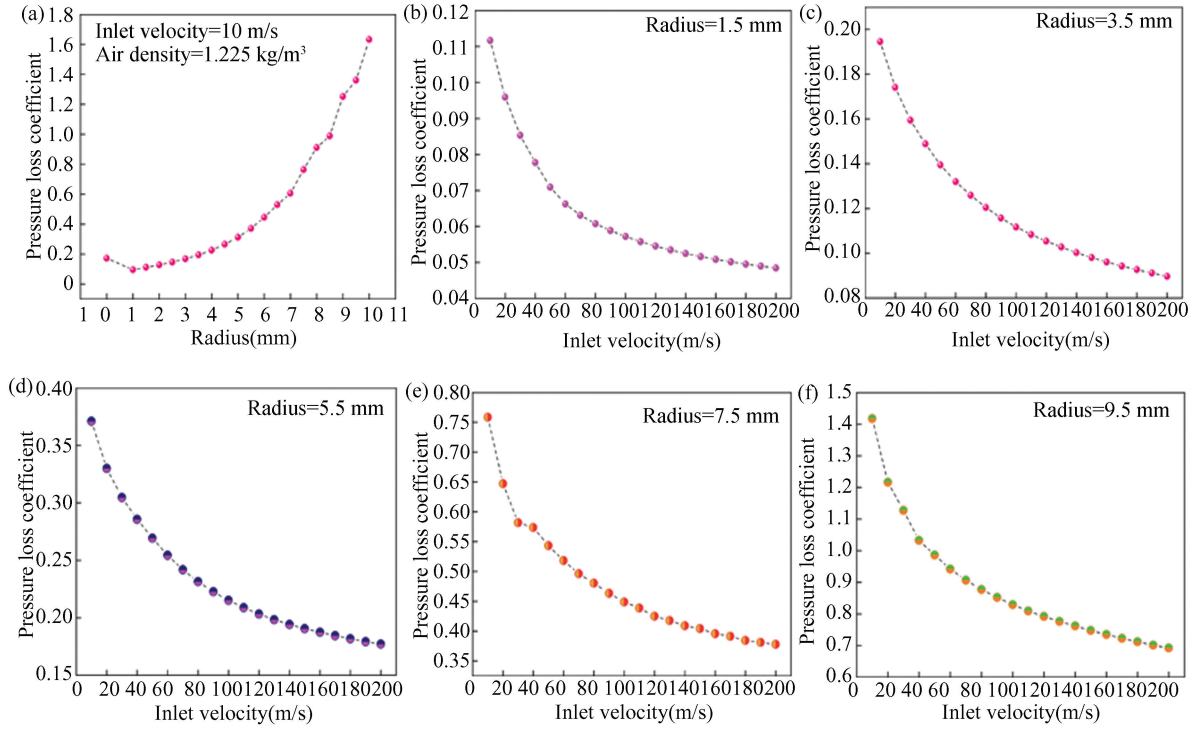

Fig.12 Variation trend of pressure loss coefficient: (a) The variation trend of pressure loss coefficient caused by deflectors with different upwind radius under the inlet speed of 10m/s; (b)-(f) When the upwind radius is 1.5, 3.5, 5.5, 7.5 and 9.5 mm, respectively, the pressure loss coefficient changes under different inlet velocity conditions

The calculation results of the empirical formula for pressure loss coefficient used in engineering are shown in Fig. 13 (a). When the calculated pressure loss coefficient is higher than 0.15, refer to the upper boundary value of the yellow area; when the calculated result is lower than 0.15, the pressure loss coefficient is determined to be 0.15 and refer to the upper boundary value of the green area. It can be seen from the calculation curve of Fig. 13 (a) that the variation trend of the pressure loss coefficient with velocity (Reynolds number) is similar to that of the curve in Fig.12 (b)-(f).

$$K = \max\left(0.10 + \frac{4.55}{\left(\lg\left(\frac{Re_{in} + Re_{out}}{2}\right)\right)^{2.58}}, 0.15\right) \tag{10}$$

where Re_{in} is Reynolds number at the inlet of the airflow; Re_{out} is Reynolds number at the outlet of the airflow. The inlet Reynolds number and outlet Reynolds number in the paper are consistent.

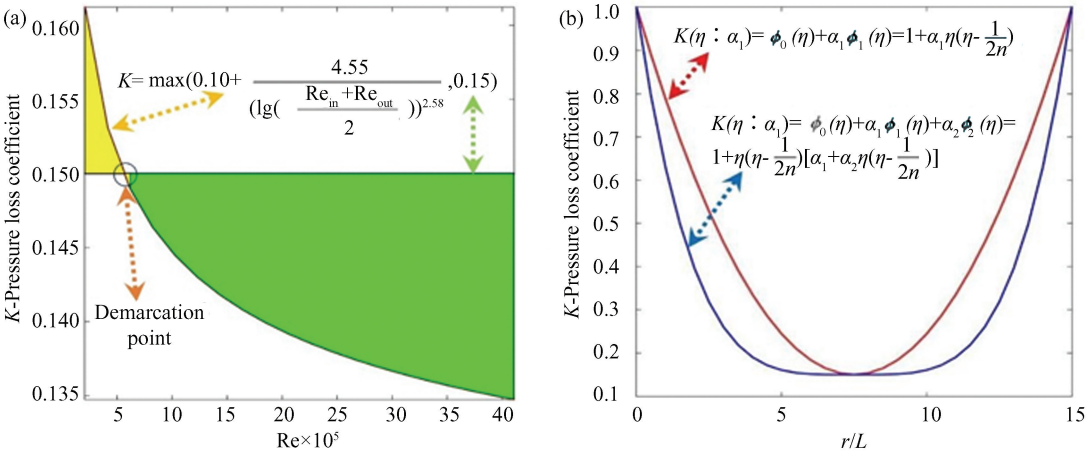

Fig.13 (a) The change curve of pressure loss coefficient calculated by engineering experience formula; (b) The variation curve of the calculated result derived from the formula

In addition to the engineering empirical formulas in relevant materials, the paper also refers to the Ritz method in the principle of minimum potential energy for calculating trial functions, and combines relevant research results to establish a new algorithm for estimating the pressure loss coefficient. To obtain a smaller pressure loss coefficient, the calculated method could be used to determine the optimal upwind size radius of the deflector under different equivalent channel size conditions.

Let $\eta = r/L$, n represents the number of deflectors, and $n = 10$ in the paper. When $\eta = 0$, there is no deflector at the corner, and the loss coefficient is large, which can be considered as $K(\eta = 0) = 1.00$. When $\eta = 1/(2n)$, the corner is completely blocked, then it is considered that the loss coefficient $K(\eta = 1/(2n)) = 1.00$.

Therefore, it can be concluded that when the upwind radius of the deflector reaches a certain value, the loss coefficient appears a minimum value. According to the assumed boundary conditions, the pressure loss coefficient is expressed as follows:

$$K(\eta; a_1) = \phi_0(\eta) + a_1\phi_1(\eta) = 1 + a_1\eta\left(\eta - \frac{1}{2n}\right) \tag{11}$$

where $\phi_0(\eta) = 1$, $\phi_1(\eta) = 0$ when $\eta = 0$ and $\eta = 1/(2n)$, hence, $\phi_1(\eta) = \eta\left(\eta - \frac{1}{2n}\right)$.

When the undetermined coefficient a_1 is the optimal solution, the loss coefficient has a minimum value, i.e., $\frac{\partial K}{\partial \eta} = 0$ and $\frac{\partial^2 K}{\partial \eta^2} > 0$.

After derivation, it is found that when $\eta = 1/(4n)$, the loss coefficient is the lowest, and referring to relevant data, the minimum loss coefficient can be assumed to be 0.15. By substituting the data into Eq. (11), $a_1 = 1360$ can be obtained.

In order to further improve contrast, increase the number of terms in the trial function, and thus improve calculation accuracy, the expression of the pressure loss coefficient is further improved as follows:

$$K(\eta; a_1, a_2) = \phi_0(\eta) + a_1\phi_1(\eta) +$$

$$a_2\phi_2(\eta) = 1 + \eta(\eta - \frac{1}{2n}) \cdot$$

$$[a_1 + a_2\eta(\eta - \frac{1}{2n})] \quad (12)$$

where $\phi_0(\eta) = 1$; When $\eta = 0$ and $\eta = 1/(2n)$, $\phi_1(\eta) = 0$ and $\phi_2(\eta) = 0$, let

$$\phi_1(\eta) = \eta(\eta - \frac{1}{2n}), \ \phi_2(\eta) = \eta^2(\eta - \frac{1}{2n})$$

When the undetermined coefficients a_1 and a_2 are the optimal solutions, the loss coefficient K appears a minimum value, so $\frac{\partial K}{\partial \eta} = 0$ and $\frac{\partial^2 K}{\partial \eta^2} > 0$ can be obtained, and by substituting them into Eq.(12), $a_1 = -2a_2\eta(\eta - 1/(2n))$, and $a_2 > 0$. Also referring to the assumptions in Eq. (11), $a_1 = 2720$ and $a_2 = 2.176 \times 10^6$ can be calculated.

The calculation results of Eqs. (11) and (12) are shown in Fig.13(b). As shown in Fig.13(b), the minimum point appears at $\eta = r/L = 1/(4n)$. By comparing Eqs.(11) and (12), it can be found that with the increase of the number of test function terms, the minimum region of the function curve gradually widens, which indicates that $\eta = r/L$ could meet the minimum requirement of the pressure loss coefficient within a certain range, providing more options for the engineering to determine the upwind radius of the deflector.

In addition to the pressure loss coefficient, the indexes to evaluate the quality of the flow field also include the velocity distribution of the flow field and the flow deflection angle distribution. Therefore, the above indexes should be considered comprehensively when selecting the upwind size of the deformable deflector. In the paper, the numerical simulation solver fluent is used to observe the distribution of velocity field and airflow deflection angle under a certain inlet velocity by changing the radius of the deflector. The Reynolds number is given as follows:

$$\mathrm{Re} = \frac{\rho v L}{\mu} \quad (13)$$

where $\rho = 1.225$ kg/m^3 (air density); $\mu = 1.7894 \times 10^{-5}$ kg/(m · s) (air viscosity); $L = 0.3$ m (feature size).

Because different velocity (Reynolds number) will have a certain effect on the flow field uniformity, and once the size of the upwind radius of the deflector is determined, it is difficult to be changed. Therefore, when studying the velocity uniformity and airflow declination distribution, the influence of the size variation of the upwind radius of the deflector on these distributions is taken as the research object. In order to comprehensively investigate the influence of the upwind size of the selected deflector on the quality of the flow field, a comprehensive judgment is made.

In Fig.14, the effect of different upwind radius deflector arrays on the uniformity of flow field velocity is shown under the condition of an inlet velocity of 10 m/s. The section 300 mm away from the pressure outlet is used as a reference position to obtain analysis data, while according to relevant standards, the central area accounting for 75% of the total cross-sectional area is generally used as the main analysis area to avoid interference with the velocity distribution analysis of the wall surface. As shown in Fig.14(a), it can be clearly observed that the airflow velocity approaches 0 near the wall position. In Fig. 14(b), the velocity distribution in the central region is shown, due to the presence of a flow deflector, the airflow passing through the deflector generates fluctuations in the velocity field. When the upwind radius of the deflector is less than 7.5 mm, the fluctuation of the velocity field is relatively similar. However, as the upwind radius continues to increase, there is no longer a regular velocity fluctuation, which also indicates that there is a significant airflow separation in the flow field at this time.

In Fig. 15, the airflow deflection angle at a section 300 mm away from the pressure outlet was calculated and analyzed, which is similar to the results of velocity uniformity analysis. When the upwind radius of the deflector is higher than 7.5 mm, as the radius size increases, the area with poor airflow deviation becomes more obvious, as shown in the yellow shaded area in the figure. In Fig. 15(b), statistical analysis was conducted on the error of airflow deflection angle in the flow field under different upwind radius deflector arrays. When the upwind radius is less than 8 mm, the error band of airflow deflection angle is between ±0.5 ° (yellow zone), which meets the relevant standard requirements. However, when the radius size exceeds 8 mm, the error band of airflow deflection angle significantly exceeds the range of ±0.5 ° (green zone).

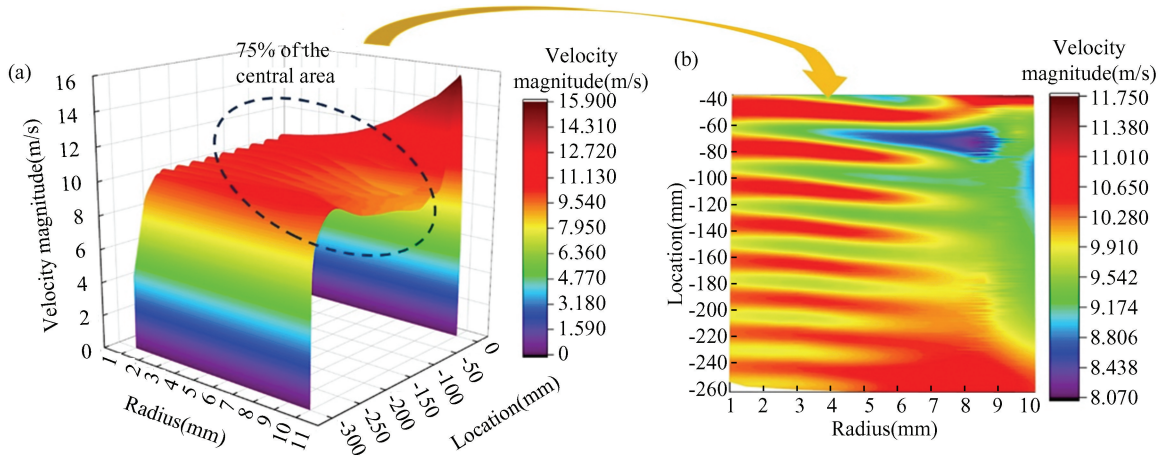

Fig.14 (a) The influence of different deflector radius on velocity distribution at 10 m/s inlet velocity; (b) Velocity distribution in the central region, which accounts for 75% of the total area

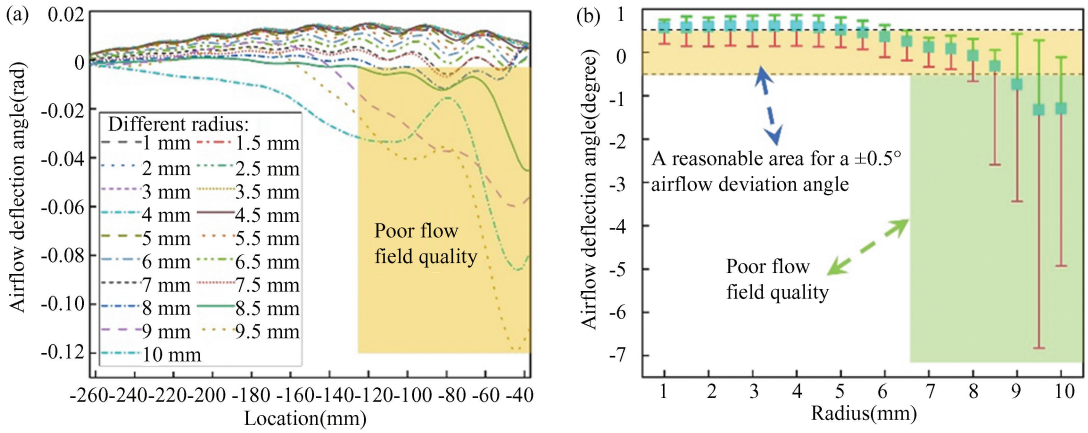

Fig.15 Distribution of flow field deflection angle under different radius deflector arrays at inlet velocity of 10 m/s; (a) Airflow deflection angle distribution at the section 300 mm away from the pressure outlet; (b) Error distribution of airflow deflection angle

In summary, when selecting the size of the upwind radius of the deflector, it is necessary to comprehensively consider indicators such as pressure loss coefficient, airflow deviation angle, and velocity uniformity.

4 Conclusions

In the paper, a deformable deflector based on smart material is designed. When the temperature of smart material reaches the glass transition temperature, the shape of the structure could be restored, so the designed deflector structure can be deformed under external excitation. The tensile and stress relaxation tests of the smart material at different temperatures and rates were carried out, thus contributing to the parameters of the relevant Maxwell viscoelastic model. On the other hand, referring to similar experimental parameters in relevant literature and combining with ABAQUS simulation software, the deformation process of the deflector was simulated, and the corresponding stress distribution at the corresponding time step was obtained, providing corresponding references for the structural optimization and preparation of deformable deflector in the future.

For the convenience of design, the following parameters are provided as references in this paper. The bending angle of the deflector prepared in this study is ca. 95 °. The research results indicate that the shape recovery rate of hinge type structures prepared based on smart materials is ca. 90%, while the heating rate is approximately 3 ℃/min, and the shape recovery time is ca. 10 min.

On the other hand, by conducting CFD numerical simulation on the deformable deflector array and deriving relevant empirical formulas, three indicators for evaluating the quality of the flow field are analyzed: pressure loss coefficient, airflow deflection angle and velocity uniformity. By numerical

simulation and theoretical calculation of flow deflectors with different speeds (Reynolds numbers) and upwind radius, a numerical evaluation model that satisfies the minimum pressure loss coefficient is established. The optimal size of the upwind radius of the flow deflector is found to produce the minimum pressure loss coefficient. Moreover, the influence of changes in velocity (Reynolds number) and upwind radius of the deflector on the flow field deflection angle and velocity uniformity is obtained, providing technical reference for selecting the upwind radius size of the deflector in engineering.

References

[1] Liu T Z, Zhou T Y, Yao Y T, et al. Stimulus methods of multi-functional shape memory polymer nanocomposites: A review. Composites: Part A, 2017, 100: 20-30. DOI: 10.1016/J.COMPOSITESA.2017.04.022.

[2] Li F, Liu Y, Leng J. Progress of shape memory polymers and their composites in aerospace applications. Smart Materials and Structures, 2019, 28(10): 103003. DOI 10.1088/1361-665X/ab3d5f.

[3] Zhao W, Liu L W, Leng J S, et al. Personalized 4D printing of bioinspired tracheal scaffold concept based on magnetic stimulated shape memory composites. Composites Science and Technology, 2019, 184: 107866. DOI: 10.1016/j.compscitech.2019.107866.

[4] Mu T, Liu L W, Lan X, et al. Shape memory polymers for composites. Composites Science and Technology, 2018, 160: 169-198. DOI: 10.1016/j.compscitech.2018.03.018.

[5] Leng J S, Wu X L, Liu Y J. Effect of a linear monomer on the thermomechanical properties of epoxy shape-memory polymer. Smart Materials and Structures, 2009, 18(9): 095031. DOI: 10.1088/0964-1726/18/9/095031.

[6] Liu Y J, Lv H B, Lan X, et al. Review of electro-active shape-memory polymer composite. Composites Science and Technology, 2009, 69(13): 2064-2068. DOI: 10.1016/j.compscitech.2008.08.016.

[7] Leng J S, Lan X, Liu Y J, et al. Shape-memory polymers and their composites: stimulus method and applications. Progress in Materials Science, 2011, 56: 1077-1135. DOI: 10.1016/j.pmatsci.2011.03.001.

[8] Liu Y J, Du H Y, Liu L W, et al. Shape memory polymers and their composites in aerospace applications: A review. Smart Materials and Structures, 2014, 23(2): 023001. DOI 10.1088/0964-1726/23/2/023001

[9] Hu J, Zhu Y, Huang H, et al. Recent advances in shape memory polymers: Structure, mechanism, functionality, modeling and applications. Progress in Polymer Science, 2012, 37(12): 1720-1763. DOI: 10.1016/J.PROGPOLYMSCI.2012.06.001.

[10] Mather P T, Luo X, Rousseau I A. Shape memory polymer research. Annual Review of Materials Research, 2009, 39: 445-471. DOI: 10.1146/annurev-matsci-082908-145419.

[11] Kunzelman J, Chung T, Mather P T, et al. Shape memory polymers with built-in threshold temperature sensors. Journal of Materials Chemistry, 2008, 18(10): 1082-1086. DOI: 10.1039/B718445J.

[12] Ratna D, Karger-Kocsis J. Recent advances in shape memory polymers and composites: a review. Journal of Materials Science, 2008, 43(1): 254-269. DOI: 10.1007/s10853-007-2176-7.

[13] Lin C, Liu L, Liu Y, et al. 4D printing of shape memory polybutylene succinate/polylactic acid (PBS/PLA) and its potential applications. Composite Structures, 2022, 279: 114729. DOI: 10.1016/j.compstruct.2021.114729.

[14] Lin C, Liu L, Liu Y, et al. Recent developments in next-generation occlusion devices. Acta Biomaterialia, 2021, 128: 100-119. DOI: 10.1016/j.actbio.2021.04.050.

[15] Lin C, Liu L, Liu Y, et al. 4D Printing of bioinspired absorbable left atrial appendage occluders: A proof-of-concept study. ACS Applied Materials & Interfaces, 2021, 13: 12668-12678. DOI: 10.1021/acsami.0c17192.

[16] Lin C, Zhang L, Liu Y, et al. 4D printing of personalized shape memory polymer vascular stents with negative Poisson's ratio structure: A preliminary study. Science China Technological Sciences, 2020, 63(4): 578-588. DOI: 10.1007/s11431-019-1468-2.

[17] Lin C, Lv J Li Y, et al. 4D-printed biodegradable and remotely controllable shape memory occlusion devices. Advanced Functional Materials, 2019, 29: 1906569. DOI: 10.1002/adfm.201906569.

[18] Xia Y, He Y, Zhang F, et al. A review of shape memory polymers and composites: Mechanisms, materials, and applications. Advanced Materials, 2021, 33: 2000713. DOI: 10.1002/adma.202000713.

[19] Zhao W, Huang Z, Liu L, et al. Porous bone tissue scaffold concept based on shape memory PLA/Fe_3O_4. Composites Science and Technology, 2021, 203: 108563. DOI: 10.1016/j.compscitech.2020.108563.

[20] Zhao W, Zhang F, Leng J, et al. Personalized 4D printing of bioinspired tracheal scaffold concept based on magnetic stimulated shape memory composites. Composites Science and Technology, 2019, 184: 107866. DOI: 10.1016/j.compscitech.2019.107866.

[21] Zhao W, Liu L, Zhang F, et al. Shape memory polymers and their composites in biomedical applications. Materials Science & Engineering C, 2019, 97: 864-883. DOI: 10.1016/j.msec.2018.12.054.

[22] Li Y. Definition and mechanical characteristics of true stress-strain. Journal of Chongqing University (Natural Science Edition), 2001, 24(3): 58-60.

[23] Zhao W. Design and Theoretical Researches of Shape Memory Tissue Scaffolds. Harbin: Harbin Institute of Technology, 2021.

[24] Yang T, Luo W, Xu P. Viscoelasticity Theory and Application. Beijing: Science Press, 2004: 13-31.